the results of three separate experiments that were conducted at varying pH values and total carbonate concentrations.

The data points indicate the absence of any response to the bicarbonate ion. Indeed, experiments carried out in mildly acidic mediums ($p\mathrm{H} < 5.5$), where bicarbonate is vastly favored over carbonate, still yield potentials appropriate for a pure carbonate response even though the concentration of carbonate is less than $10^{-8}M$. In practical terms, however, the interconversion of carbonate with bicarbonate restricts the lower pH limit of the electrode to approximately pH 5.5. The electrode has an upper pH limit of approximately 8.5 at $4 \times 10^{-3}M$ carbonate and 9.5 at $5 \times 10^{-2}M$ carbonate.

Measurements carried out in mixtures of carbonate and chloride show negligible chloride interference even in samples containing $10^{-1}M$ chloride and $10^{-5}M$ carbonate. We calculate (*6*) the selectivity of carbonate to chloride of the electrode to be 5.4×10^3. This value should be regarded as a lower limit because of possible residual amounts of carbonate in the chloride reagent used. Similarly, we have determined the selectivity of carbonate to sulfate of the electrode as 6.7×10^3 and that of carbonate to phosphate (taken as HPO_4^{2-}) as 3.8×10^3.

The overall potentiometric behavior of the new electrode is typical of liquid membrane electrodes in general. We observe response times ranging from 30 seconds to 2 minutes in carbonate solutions, the slowest response being found at the lowest concentrations. Electrical noise in carbonate solutions does not exceed 0.2 mv, and a reproducibility of ± 0.5 mv from sample to sample is readily achieved. The electrode lifetime in routine use will depend on such factors as the specific support membrane used and solution conditions, but it appears to be consistent with that reported for liquid membrane electrodes in general (*2*). In view of the dynamic range, selectivity, and other properties of this electrode, we expect it to be useful for carbonate measurements in biological, chemical, and oceanographic samples.

H. B. HERMAN*
G. A. RECHNITZ

Department of Chemistry,
State University of New York,
Buffalo 14214

References and Notes

1. A. L. Grekovich, E. A. Materova. N. V. Garbuzovz, *Zh. Anal. Khim.* **28**, 1206 (1973); C. J. Coetzee and H. Freiser, *Anal. Chem.* **41**, 1128 (1969); W. M. Wise, U.S. Patent No. 3,723,281 (27 March 1973).
2. J. W. Ross, in *Ion-Selective Electrodes*, R. A. Durst, Ed. (National Bureau of Standards Special Publication No. 314, Washington, D.C., 1969), chap. 2.
3. J. H. Simons, W. T. Black, R. F. Clark, *J. Am. Chem. Soc.* **75**, 5621 (1953).
4. H. C. Helgeson, *J. Phys. Chem.* **71**, 3121 (1967).
5. C. W. Davies, *Ion Association* (Butterworth, London, 1962), p. 41.
6. K. Srinivasan and G. A. Rechnitz, *Anal. Chem.* **41**, 1203 (1969).
7. Research supported by the Environmental Protection Agency.
* On leave from the Chemistry Department, University of North Carolina, Greensboro 27412.

31 January 1974; revised 27 March 1974

Equatorial Jet in the Indian Ocean: Theory

Abstract. *A nonlinear numerical model and a simple analytical theory explain the basic features of the equatorial surface jet in the Indian Ocean recently reported by Wyrtki. The observed width of this transient current, 500 kilometers, is given theoretically by twice the baroclinic equatorial radius of deformation. The numerical model reproduces all Wyrtki's observations of this natural phenomenon.*

During the transition periods between the two monsoon seasons, a narrow, high-speed surface jet flows along the equator from west to east across the entire Indian Ocean (*1*). We have been developing numerical models of the eastern boundary layer (*2, 3*) to study coastal upwelling. Wyrtki's report (*1*) encouraged us to use our model to explain the physics of this transient, wind-driven jet. In this report we derive theoretical estimates of the observed space and time scales given by Wyrtki.

In the numerical model the nonlinear, time-dependent primitive equations are solved for a two-layer, flat-bottomed ocean on a beta plane (*4*). The independent variables are x (distance eastward), y (distance northward), and t (time). The dependent variables are the eastward and northward horizontal velocity components, u and v, respectively, and the thickness, h, of each layer. The equations are

$$\begin{aligned}
&\frac{\partial \mathbf{v}_1}{\partial t} + \mathbf{v}_1 \cdot \nabla \mathbf{v}_1 + \mathbf{k} \times f\mathbf{v}_1 = -g\nabla(h_1 + h_2 + D) + (\tau^s - \tau^I)/\rho h_1 + A\nabla^2\mathbf{v}_1 \\
&\frac{\partial h_1}{\partial t} + \nabla \cdot h_1\mathbf{v}_1 = 0 \\
&\frac{\partial \mathbf{v}_2}{\partial t} + \mathbf{v}_2 \cdot \nabla \mathbf{v}_2 + \mathbf{k} \times f\mathbf{v}_2 = -g\nabla(h_1 + h_2 + D) + g\frac{\Delta\rho}{\rho}\nabla h_1 + (\tau^I - \tau^B)/\rho h_2 + A\nabla^2\mathbf{v}_2 \\
&\frac{\partial h_2}{\partial t} + \nabla \cdot h_2\mathbf{v}_2 = 0 \\
&\mathbf{v}_i = [u_i, v_i]
\end{aligned} \tag{1}$$

where f is the Coriolis parameter; g is the acceleration of gravity; D is the height of the bottom topography above a reference level; τ^s, τ^I, and τ^B are the wind, interfacial, and bottom stresses; ρ is the density of the ocean; $\Delta\rho$ is the density difference between the layers; and A is the horizontal eddy viscosity.

These equations are well known, as are the details of their derivation (*2*). In this report we discuss a numerical solution of these equations and a simple analysis of a "stripped-down" linear version of this model.

Before presenting numerical results, we consider the simplest model of equatorial surface currents for the middle of the Indian Ocean, away from boundaries. If we let $u = u_1 - u_2$, $v = v_1 - v_2$, and $h = h_1$, Yoshida (*5*) has shown that the equations

$$\begin{aligned}
\frac{\partial u}{\partial t} &= \beta y v + \tau_x^s/\rho H_1 \\
\beta y u &= -(g\Delta\rho/\rho)\frac{\partial h}{\partial y} \\
\left(\frac{1}{H_1} + \frac{1}{H_2}\right)\frac{\partial h}{\partial t} &= -\frac{\partial v}{\partial y}
\end{aligned} \tag{2}$$

may be used to deduce some understanding of the physics (*6*). In Eqs. 2, β is the coefficient of the latitude variation of f, τ_x^s is the x component of τ^s, and H is the initial value of h (capital letters denote initial values).

When τ_x^s is a constant, impulsively applied, the north-south velocity, v, is a solution of the ordinary differential equation

$$L^4 \frac{\partial^2 v}{\partial y^2} - y^2 v = aLy \tag{3}$$

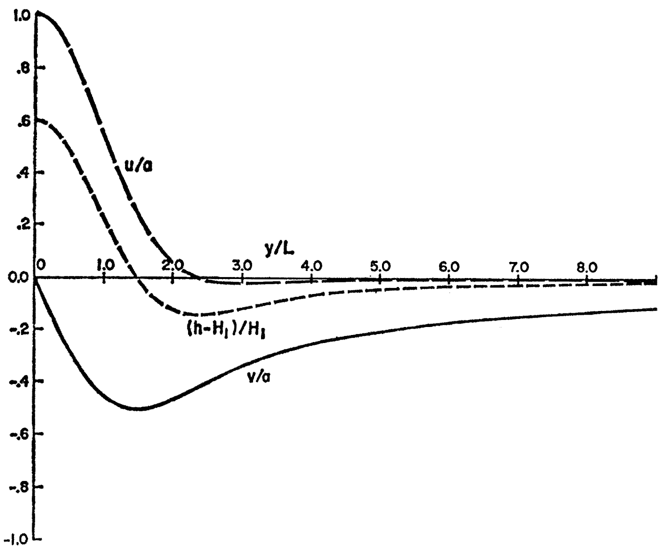

Fig. 1. Solution to the linear model in nondimensional units. The eastward jet, u/a, and the pycnocline anomaly, $(h - H_1)/H_1$, are plotted at time $(\beta L)^{-1}$. The jet flow decays to zero near $2L$; a weak westward flow is calculated from $2.3L$ and northward.

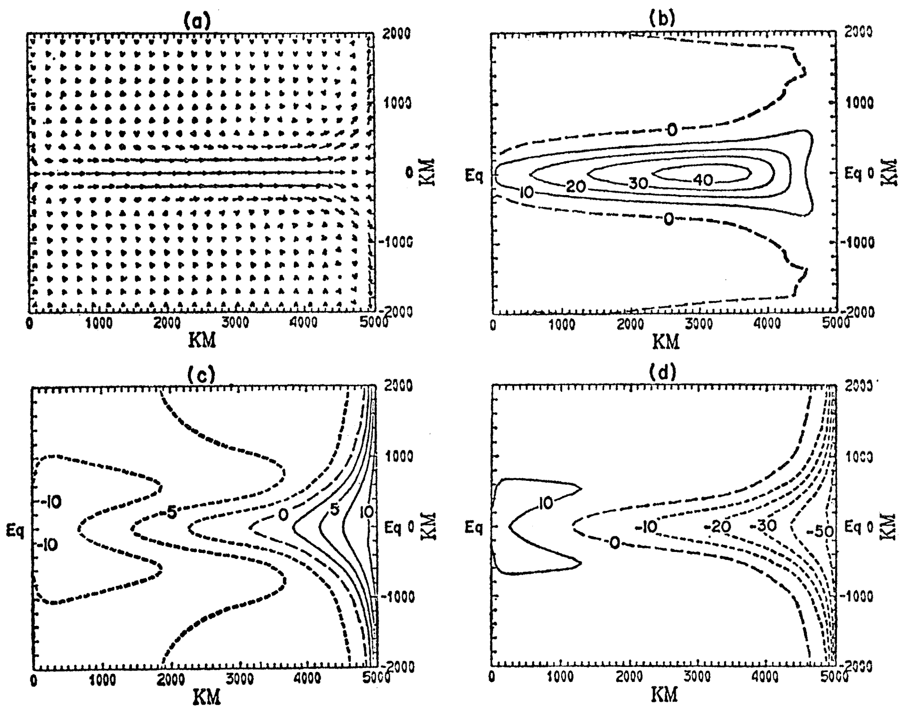

Fig. 2. Numerical solution at day 30. (a) Upper-layer transport vectors ($h_1\mathbf{v}_1$). The Ekman transport enters the equatorial region and then flows eastward in a strong equatorial jet. Along the eastern boundary the current flows north and south away from the equator in a narrow coastal jet. (b) Distribution of u_1; the maximum eastward flow is 45 cm sec^{-1}. (c) Rise (fall) of the thermocline from 120 m. This interface has risen 15 m in the west and fallen over 50 m along the eastern boundary. (d) Height (in centimeters) of the free surface above mean water level. There is a tilt of 20 cm across the basin.

The fundamental scale length, L, is known as the baroclinic equatorial radius of deformation. Time-dependent, baroclinic ocean motions always depend on the deformation radius. Here

$$L = (C/\beta)^{1/2}$$

$$C = \left[g \frac{\Delta\rho}{\rho} H_1 H_2/(H_1 + H_2) \right]^{1/2}$$

$$a = \tau_x^s/\beta L H_1 \rho$$

where C is the internal gravity wave speed. We expect a priori that the dominant baroclinic motions will be confined to within a distance L of the equator in the ocean interior. The solution to Eqs. 2 is illustrated in Fig. 1.

The measured values (or estimates) of these constants are $\beta = 2.25 \times 10^{-13}$ cm^{-1} sec^{-1}, $\Delta\rho/\rho = 0.003$, $H_1 = 10^4$ cm, and $H_2 > 4H_1$; thus, $L = 277$ km. Since the equatorial jet is symmetric about the equator, the width, $2L$, agrees quite well with Wyrtki's estimate of 500 km. The width of the jet is independent of the shape and strength of the wind field.

Equation 3 implies that far from the equator

$$v = - \tau_x^s/\beta y \rho H_1$$

which is the classical Ekman drift solution. Near the equator, v approaches zero. Thus, from Eqs. 2, the eastward jet is driven directly by the wind stress. If the wind acts for 20 days at 0.5 dyne cm^{-2}, we can expect the surface velocity to approach 100 cm sec^{-1}. These estimates from the linear theory agree with the observations (*1*). After approximately 10 days, the linear model is invalid since substantial east-west pressure gradients develop. The numerical model does not have this deficiency.

The complete nonlinear numerical model was solved for a 5000-km-wide basin with rigid walls on the east and west and open north-south boundaries (*3*). The model was driven from rest by a uniform west wind. The wind stress tended to 0.5 dyne cm^{-2} with a time constant of 2 days. The ocean was initially at rest; $h_1 = 120$ m, $h_2 = 480$ m, and $A = 10^6$ cm^2 sec^{-1}. The numerical techniques are described elsewhere (*2, 3*).

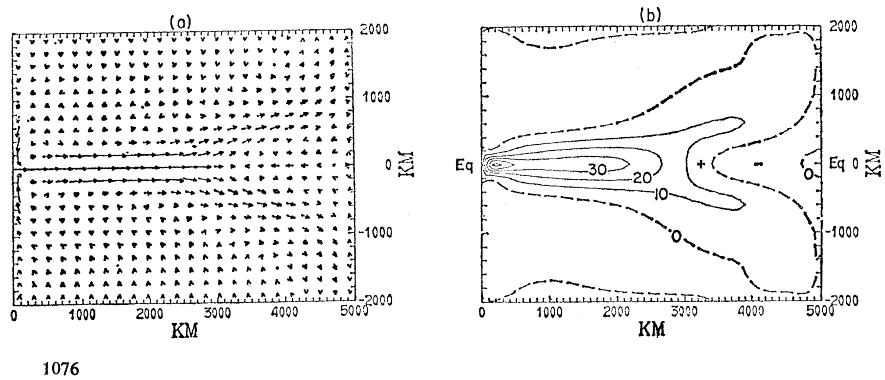

Fig. 3. (a) Upper-layer transport after 60 days. A westward equatorial flow exists in the eastern ocean. The eastward-flowing jet leaves the equator at 3000 km and flows north and south. (b) East-west velocity, u_1. The jet maximum (50 cm sec^{-1}) is near the western boundary.

The model has been integrated by using various wind patterns for over 75 days. In this short report we cannot properly present the model output. Instead, we choose to present distributions of $u_1(x,y)$ at 30 and 60 days, $h_2 - H_2$ (the pycnocline anomaly) at 30 days, and the free surface anomaly at 30 days. The upper layer transports are shown for 30 and 60 days.

After 30 days a narrow jet is well developed over the entire equatorial ocean (Fig. 2). The numerical grid was chosen such that all boundary currents are well resolved in the computations. This was accomplished by using a variable resolution grid (*3*). The equatorial jet reached a speed of 45 cm sec^{-1} after 30 days. The tilt of the ocean surface is 20 cm across the basin, as observed by Wyrtki (*1*). The flow has induced upwelling in the western ocean and downwelling near the eastern boundary.

After 2 months the jet has reached a strength of 50 cm sec^{-1} (Fig. 3) but the maximum has migrated far westward. The upper-layer flow shows a very interesting pattern. At the equator in the eastern third of the basin the pressure gradient is balanced by the wind stress. The surface current has reversed and flows westward. The equatorial jet separates from the equator at 3000 km and flows north and south in two narrow, strong (> 10 cm sec^{-1}) currents. Wyrtki does not report this current.

The thermocline (pycnocline) anomaly calculated after 60 days indicates a 25-m rise in the western ocean and a 45-m drop in the eastern ocean. These are very close to the rise and fall of the 20°C isotherm observed by Wyrtki. The tilt of the ocean surface is not shown after 60 days since the mean east-west tilt remains about 20 cm.

We have not shown the flow structure in the lower layer. It is interesting to note that the depth-averaged velocities are small, no more than 3 cm sec^{-1}. This implies that the currents seen in Figs. 2 and 3 are reversed in direction in the lower layer.

Each of Wyrtki's observations has been simulated in the numerical model. A more detailed report and interpretation of this simulation will be reported elsewhere (*7*).

JAMES J. O'BRIEN
H. E. HURLBURT*
Departments of Meteorology and Oceanography, Florida State University, Tallahassee 32306

References and Notes

1. K. Wyrtki, *Science* **181**, 262 (1973).
2. J. J. O'Brien and H. E. Hurlburt, *J. Phys. Oceanogr.* **2**, 14 (1972); H. E. Hurlburt and J. D. Thompson, *ibid.* **3**, 16 (1973); R. T. McNider and J. J. O'Brien, *ibid.*, p. 258.
3. The numerical model developed by H. E. Hurlburt [thesis, Florida State University (1974)] was used for these computations. The details of the open boundary conditions, the variable mesh, numerical scheme, and so forth, are described in Hurlburt's thesis.
4. The Coriolis parameter, f, which depends on the sine of the latitude, is approximated by a linear function, $f_0 + \beta y$, where f_0 is a reference value (here 0) and Cartesian coordinates are used.
5. K. Yoshida [*J. Oceanogr. Soc. Jap.* **15**, 159 (1959)] first derived Eqs. 2 and the solutions in Fig. 1.
6. A. E. Gill (preprint) discusses a model for the westward surface currents and eastward undercurrent which are found in the Pacific and Atlantic oceans. The extension to this Indian Ocean case is trivial; our contribution here is the numerical solution. G. Philander [*Rev. Geophys.* **11**, 513 (1973)] has reviewed the evidence for the westward-flowing equatorial jet found in the equatorial Pacific and Atlantic.
7. J. J. O'Brien and H. E. Hurlburt, in preparation.
8. Supported by the Office of Naval Research, Ocean Science and Technology Branch. Partial support was derived from Coastal Upwelling Ecosystems Analysis, a program of the International Decade of Ocean Exploration, NSF grant GX-33502. The numerical work was done at the National Center for Atmospheric Research, which is supported by the National Science Foundation. Partial computer support was provided by the computer center, Florida State University. This is Contribution No. 98 of the Geophysical Fluid Dynamics Institute, Florida State University.
* Present address: Advanced Study Program, Box 3000, National Center for Atmospheric Research, Boulder, Colorado 80303.

26 December 1973; revised 8 March 1974

Satellite Photograph Presents First Comprehensive View of Local Wind: The Santa Ana

Abstract. *The photograph of the 1 January 1973 Santa Ana wind condition reveals local atmospheric dynamics rarely recorded on satellite imagery. The Santa Ana wind implies very specific weather conditions for the Los Angeles coastal lowland. Destructive land uses, in part, provided the material visible in the dust plumes.*

Images sensed by the National Aeronautics and Space Administration's Earth Resources Technology Satellite (ERTS-1), orbiting 855 km above the earth, in January 1973 dramatically recorded a Santa Ana wind condition in Southern California (Fig. 1). The image shown is a mosaic of two returns taken on 1 January 1973 in band 7 (0.8 to 1.1 μm). The San Gabriel Mountains, bounded on the north by the San Andreas fault, angle across the lower portion of the image; the Mojave Desert is seen in the middle, and the Garlock fault, which separates the Mojave from the Sierra Nevada and Great Basin, is shown in the upper portion of the picture (see map inset in Fig. 1). The dust plumes in the Mojave are 10 to 30 km in length and cover a landscape of 300 km^2. A Santa Ana wind results in particular weather conditions, and its ramifications are important to both agriculturalists and conservationists.

A Santa Ana (a foehn type wind) may develop in Southern California after the passage of a cold front in central California and Nevada. A mass of stagnant air settles over the Great Basin, developing a deep high-pressure cell. Air flows from the cell across the Mojave Desert and spills over the Southern California Mountains into the coastal lowland of the Los Angeles Basin. Cool temperatures prevail in the Mojave, but, as the air flows downslope and through the canyons of the San Gabriel, San Bernardino, and Santa Ana mountains, it warms and dries adiabatically. As a result high winds, unseasonably warm temperatures, and low humidities develop in the Los Angeles (*LA*) Basin. In addition, the danger of brush fires increases, crop damage is likely, and the relatively open desert environment is susceptible to increased wind erosion and damage.

On 1 January at the Santa Monica (*SM*) Pier (elevation, 4.6 m) a maximum temperature of 21.1°C (70°F) was reached while at Palmdale (*P*) (elevation, 767 m), in the Mojave Desert, a maximum temperature of 11.7°C (53°F) was attained. Wind velocities during a Santa Ana are comparatively high. For example, at Riverside (*R*), a daily wind total (*1*) of 269 km was recorded on 1 January, and on the following day, a continuation of the Santa Ana condition, a daily wind total of 268 km was reached. For the next 7 days, as the Santa Ana subsided, daily wind totals of 61, 73, 60, 30, 18, 15, and 13 km, respectively, were recorded at Riverside. Because the low-level inversion layer that contributes to air stagnation in the Los Angeles Basin could not develop, visibilities were virtually unlimited in many locations in the Los Angeles metropolitan area.

During a Santa Ana, which may last